Quantitive Harmonic Analysis and Force Ripple Suppression of a Parallel Complementary Modular Linear Reluctance machine

Zhenghao Li, Shuangxia Niu, Xing Zhao and W. N. Fu

***Abstract*— Considering the fluctuating price of permanent magnet, magnetless machine is a new trend in development. Variable reluctance linear machines (VRLM) with simple structure, good robustness, and high dynamic performance, is one of the potential candidates for linear direct-drive wave energy conversion (WEC) application replacing PM-excited linear machine. To ameliorate the fault-tolerance performance of VRLM, the researchers have come up with modular or segmented design, denoted as modular variable reluctance linear machines (MVRLM) However, suffering from large thrust ripple, the design of MVRLM still needs to be improved. To relieve the force ripple of MVRLM, a novel H-shaped modular variable-flux linear reluctance machine (HMVF-LRM) is proposed in this paper. The principle of force ripple suppression by using parallel-complementary structure is analyzed deeply. In this paper, the analytical calculation of induced voltage is developed quantitively with equivalent magnetic circuit method (EMC) and harmonics analysis. Then the design mechanism of HMVF-LRM is illustrated. Further, the performance and fault-tolerant capability of the proposed machine are simulated and evaluated by finite element analysis (FEA), and the prototype is tested to verify the effectiveness of the machine design.**

***Index Terms*—Complementary Structure, Modular Design, Linear Machine**

I. INTRODUCTION

WAVE energy conversion (WEC) devices are the equipment to capture the energy produced by wave energy and convert this mechanical energy into electrical power. Permanent magnet linear machine (PMLM) is conventionally used as generators in WEC system [1]. However, considering the fluctuating price of permanent magnet, the non-magnetic or magnetless machines for WEC have drawn attentions of researchers [2].

Variable reluctance linear machines (VRLM), which are driven by the variations of reluctance, have the merits of low cost, easy voltage regulation, and good robustness, are potential candidates for direct-drive WEC generators as a magnetless machine. Since completely magnet-free, they are easy to manufacture, install and maintain. In terms of the excitation methods, VRLM can be divided into DC excitation variable flux linear reluctance machine (DCE-VFLRM) [2], switched reluctance linear machine (SRLM) and synchronous linear reluctance machine (Syn-LRM). SRLM has been well investigated for years, which has advantages of higher power density but results in complicated driving method and large thrust ripple [3-4]. In comparison, Syn-LRM has relatively easy driving method, but its thrust density is limited as a direct-drive machine [5]. DCE-VFLRMs have relieved the thrust ripple of the machines and take advantages of simple manufacture and low cost. However, they still suffered from lower thrust density considering its unipolar flux in the primary core [6-7]. To ameliorate the performance of VRLM, the researchers have come up with various solutions and modular or segmented design is one of them. Modular design, which decoupled mutual inductances between different phases, is an effective method to improve efficiency and improve fault tolerance [8]. The state of art of these modular VRLMs is provided as follows.

Modular primary design is firstly applied to rotary switched reluctance machine [9]. After that, segmented secondary design [10-11], multitoothed modular design [12] and complementary modular design [13] are also proposed to improve its output thrust force performance. However, SRLM still suffered from high thrust force ripple, complicated control methods and acoustic noise. To relieve force ripple and achieve the simplicity in driving in modular VRLMs, a U-shaped design has been applied to DCE-VFLRM, and its winding configuration and slot/ pole combination impact is discussed [14]. U-shaped core design inevitably reduced the utilization ratio of excitation because of the relatively lower winding factor [15]. Therefore, an E-shaped modular machine with higher winding factor is proposed [16]. [17] proved that multi-toothed modular machines with DC excitation achieve better thrust performance but result in complicated manufacturing process. In [17], the equal clearance method designed for modular machine, which keeps a certain distance between different modules, is adopted to suppress the ripple.

At present, apart from forementioned equal clearance method, complementary design is constructed to further relieve the thrust ripple problem. Complementary design is accomplished via dual-sided structure to address ripple issues, which can be classified into series and parallel complementary. Series complementary structures have been discussed in depth in the yokeless machine, whose complementary structure is constructed via mover and two stator yokes [18]. In contrast, machines with parallel-complementary design, whose two complementary parts work independently can be proved to be more reliable and achieve lower thrust ripple [19]. A claw-shaped modular design is applied to electrically-excitation doubly salient machine to relieve the output ripple [20]. Up till now, fewer research works investigating modular design of

VRLM, especially DCE-VFLRM, are carried out, indicating more research is necessary.

In light of the existing works on modular VRLMs, there are mainly following problems existed in these machines.

(1) Few works concentrated on the quantitative analysis of the spatial harmonics are reported.

(2) Some design guidelines on the selection of the parameters of the machines have not specifically provided.

(3) Saturation problems still exist in the primary core of the machine, which hinder its further application.

(4) Due to the limited length of each module, the thrust ripple of the machines is relatively high.

In this paper, to solve these issues, a novel H-shaped modular variable flux linear reluctance machine (HMVF-LRM) with a parallel-complementary design is proposed to improve the quality of the generated power and relieve the saturation problems in the primary core. The working principle and design mechanism of the HMVF-LRM are also investigated in a quantitative method. In section II, the machine structure of it is introduced, and the working principles are investigated based on the equivalent magnetic circuit (EMC) and harmonic analysis. Section III discussed the optimal slot-pole combinations for modular design. Section IV specifically investigated the performance of the machine with/ without complementary design, including induced voltage, output thrust, efficiency, etc. The prototype of the machine is manufactured and tested in Section V. The FEM and experimental results are compared to validate the effectiveness.

II. Machine Structure and Working Principle

A. Machine Structure and Redundant Generation System

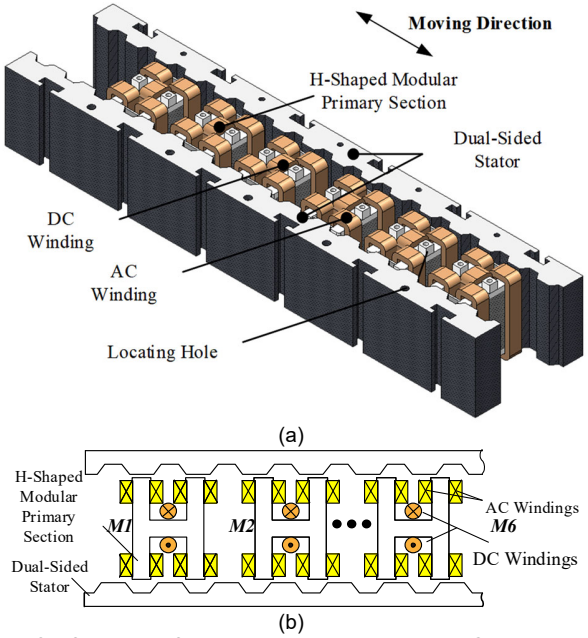

Fig. 1. Configuration of HMVF-LRM. *(a) 3D model. (b) Cross section.*

Due to the flux leakage in conventional VF-LRM, the utilization of DC field windings is relatively low, and the output torque ripple is relatively large [2]. Fig. 1(a) depicts the 3D model of the proposed machine and Fig. 1(b) demonstrates the cross-section of it. The primary part is consisted of 6 separated modules, whose magnetic-path connection between neighbouring modules is cut off, and the secondary part adopts a dual-sided salient-pole tooth. Each modular primary part of the proposed machine adopts an H-core design, and applies a double-layers winding design. On the other hand, DC windings wound on the yoke of primary part in each module have the same polarity. The secondary stators locate on both sides of the mover, which stagger π electrical angle shift. The design features of the proposed HMVF-LRM can be summaries as follows,

a) The H-shaped modular design could simplify the manufacture and assembly process of the machine.

b) The π electrical angle shift between the two stators constructs a parallel complementary magnetic path.

c) The concentrated field winding wound around is employed in the primary part to improve DC utilization.

The whole generation system is designed to be redundant properly to improve the fault tolerance of the system, which is shown in Fig. 2. The inverter unit utilizes a full H bridge for field winding. Meanwhile, uncontrollable redundant converter (URC) sets are utilized, which adopt independent H-bridged uncontrollable converters and facilitate the generator to achieve higher fault-tolerant capability and flexibility. After that the generated power is stored in the isolated battery and transmitted to power grid via DC/AC inverter.

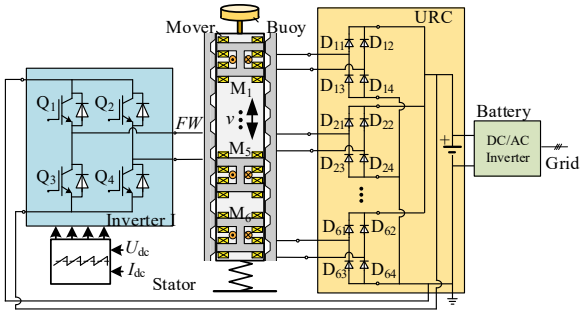

Fig.2. Redundant generation system for WEC.

B. EMC Analysis of H-shaped Modular Core

At the position in Fig. 3(a), the mover teeth align with the upper salient pole teeth, and the flux generated by the upper conductors of DC windings go through coil A_{11}, Stator 1, and coil A_{12} to form the loop, which is demonstrated as the blue dash. On the other side, flux linkages in coil A_{21} and coil A_{22} drop to minimum value due to the large reluctance. Vice versa, at the position of Fig. 3(b), fluxes in A_{21} and A_{22}, shown as the red dash line, reach the top value in opposite direction. According to equivalent magnetic circuit (EMC) shown in Fig. 4(a), there are two symmetric magnetic return paths for the DC winding excitation ϕ_{dc}, where R_{sy} and R_{st} are the reluctance of stator yoke and stator teeth respectively, R_{my} is the mover yoke reluctance, R_{g1} and R_{g2} are air-gap reluctance at both sides, and the values of them are varied periodically according to relative mover's displacement. Fig.4 (b) illustrates the waveform of air-gap reluctance R_{g1} and R_{g2}. As shown in Fig.4 (b), the amplitudes of R_{g1} and R_{g2} are the same, but a change in the opposite direction. Therefore, the value of R_{g1} and R_{g2} can be expressed as (1),

$$R_{g1,2} = R_{g0} \pm \Delta R_g(x) \tag{1}$$

where R_{g0} is the constant component of air gap reluctance $R_{g0}=\Lambda_{air}^{-1}w_{st}^{-1}(g+h_{st}/2)$, $\Delta R_g(x)$ is the variable component with respective to displacement of mover and $|\Delta R_g(x)|=\Lambda_{air}^{-1}w_{st}^{-1}h_{st}/2$, Λ_{air} is the permeability of air, w_{st} is the width of stator teeth, h_{st} is the height of stator teeth, and g is the length of air gap. The main flux ϕ_m can be solved using the mesh current method, which is expressed as follows,

Loop1:

$$(2R_{mt}+2R_{g1}+R_{sy})\phi_{m1}+R_{my}(\phi_{m1}+\phi_{m2})=F_{dc} \quad (2\text{-a})$$

Loop2:

$$(2R_{mt}+2R_{g2}+R_{sy})\phi_{m2}+R_{my}(\phi_{m1}+\phi_{m2})=F_{dc} \quad (2\text{-b})$$

Solving (2), main flux ϕ_m of the winding in both sides of airgap can be expressed with following equations,

$$\phi_{m1,2}=\frac{R_{my}-R_{2,1}}{R_{my}^2-R_2R_1}F_{dc} \quad (3)$$

where $R_1=2R_{mt}+2R_{g1}+R_{my}+R_{sy}$; $R_2=2R_{mt}+2R_{g2}+R_{my}+R_{sy}$.

Furtherly, the main flux could be expressed as follows, with complementary structure,

$$\phi_m=\phi_{m1}-\phi_{m2}=\frac{-2\Delta R_g}{R_{my}^2-R_{g0}^2+\Delta R_g^2}F_{dc} \quad (4\text{-a})$$

without complementary structure,

$$\phi_m=\phi_{m1}+\phi_{m2}=\frac{2\left(R_{my}-R_{g0}+\Delta R_g\right)}{R_{my}^2-\left(R_{g0}+\Delta R_g\right)^2}F_{dc} \quad (4\text{-b})$$

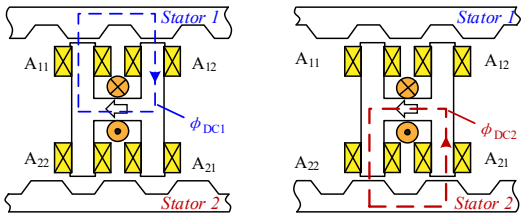

(a) (b)

Fig.3. Operation principle. *(a) Position a. (b) Position b.*

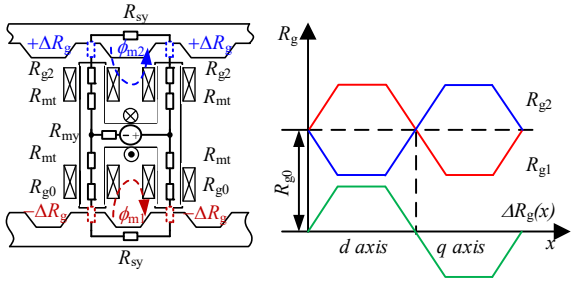

(a) (b)

Fig.4. Simplified EMC. *(a) EMC model. (b) Reluctance waveform.*

To facilitate calculation, R_1 and R_2 are divided into constant and variable parts, rewritten as, $R_1=R_0+\Delta R_g(x)$ and $R_2=R_0-\Delta R_g(x)$ for parallel- complementary design, and $R_{1,2}=R_0+\Delta R_g(x)$ for non-complementary design. Substituting this to (3), the equation of main flux can be derived. Comparing the amplitude of main flux $|\phi_m|$ with/without parallel-complementary structure, denoted as ϕ_m/ ϕ'_m, enhancement index δ can be defined as,

$$\delta=\frac{|\phi_m|}{|\phi'_m|}=\frac{(R_0+R_{my})^2-|\Delta R_g|^2}{R_0^2-R_{my}^2-|\Delta R_g|^2}\geq 1 \quad (5)$$

Therefore, after applying parallel-complementary structures, the amplitude of the main flux linkage can be boosted, when the reluctance of mover yoke cannot be neglected. Under no-load or light-load situation, when $R_{my}<<R_0$, the enhancement index δ is approximately equal to 1. As load increases, however, the reluctance R_{my} increases as well, which tends to be equal to $R_0-\Delta R_g$, and the enhancement index δ has been increased to $2+2R_{my}/\Delta R_g$, indicating that the proposed complementary structure can improve the main flux linkage over twice under the heavy-load situation.

C. Quantitive Harmonic Analysis

Each module of the mover forms a pair of magnetic poles, as illustrated in Fig.5. The distribution function of MMF of DC current F_{dc} shown in Fig.5 can be expressed as (6),

$$F_{dc}(x)=\sum_{h=1,3,5}\frac{4F_{max}}{h\pi}\sin(h\frac{\pi}{\tau_{dc}}x) \quad (6)$$

where h is the order of DC harmonics, F_{max} is the maximum value of MMF, and τ_{dc} is the pole pitch of DC excitation. As the dc excitations in each module are the same, τ_{dc} equals to the pole pitch of module τ_m denoted in Fig. 5.

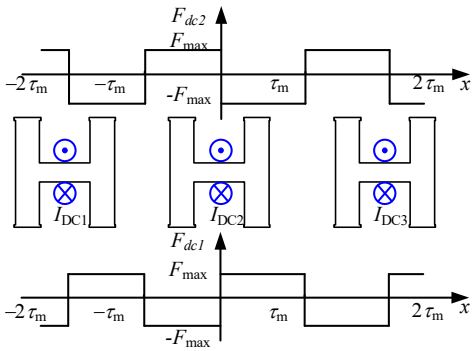

Fig.5. MMF generated by DC excitation.

Assuming that $\Lambda_{s1}(x,t)$ is permeance function of one side of air gap and can be expressed as (7),

$$\Lambda_{s1}(x,t)=[\Lambda_0+\sum_{n=1,2...}\Lambda_n\cos(\frac{n\pi}{\tau_s}(x+v_m t))] \quad (7)$$

where Λ_0, Λ_n is the coefficient of air gap permeance function of the stator side for the average component and n^{th} harmonics, τ_s is the pole-pitch of the secondary tooth, and v_m is the mechanical speed of the mover. Given the symmetric structure of proposed machine, the flux density excited by DC in both sides of air-gaps $B_{dc1}(x,t)$, $B_{dc2}(x,t)$ are deduced by (8) and (9). The excitation flux densities in the airgap is the sum of the three components, $B_{dc1(0)}$, $B_{dc1(+)}$ and $B_{dc1(-)}$ represent the excitation flux densities without/with flux modulation.

$$\begin{cases} B_{dc1}(x,t)=F_{dc}(x)\cdot\Lambda_{s1}(x,t)=B_{dc1(0)}+B_{dc1(+)}+B_{dc1(-)} \\ B_{dc1(0)}(x)=\sum_{h=1,3,5}B_{h,0}\sin\left(\frac{2\pi}{L_x}\cdot hP_{dc}x\right), \\ B_{dc1(\pm)}(x,t)=\sum_{n=1,2,3...}\sum_{h=1,3,5...}B_{h,n} \\ \cdot\sin\left\{\frac{2\pi}{L_x}\left[(hP_{dc}\pm nP_s)x\pm nP_s v_m t\right]\right\}, \end{cases} \quad (8)$$

where P_{dc} is the PPN of excitation field without modulation, P_s is the PPN of secondary teeth aligning with mover, L_x is the length of the mover in x-axis direction and $B_{h,n}$ is the

coefficients of the flux densities. Similarly, $B_{dc2}(x, t)$ can be deduced as following (8),

$$\begin{aligned} B_{\mathrm{dc2}}(x,t) &= -F_{\mathrm{dc}}(x)\cdot\Lambda_{\mathrm{s2}}(x,t) \\ &= -F_{\mathrm{dc}}(x)\cdot\Lambda_{\mathrm{s1}}(x,t+\tau_{\mathrm{s}}/v_m) \end{aligned} \tag{9}$$

TABLE I HARMONICS OF FLUX DENSITIES IN AIR GAP

	Spatial Order	Amplitude	Speed
I	$h\frac{\pi}{\tau_{dc}}$	$\frac{4F_{\max}}{h\pi}\Lambda_0$	0
II	$\left\|h\frac{\pi}{\tau_{dc}}-n\frac{\pi}{\tau_s}\right\|$	$\frac{1}{2}\cdot\frac{4F_{\max}}{h\pi}\Lambda_n$	$-\frac{n\pi/\tau_s}{h\pi/\tau_{dc}-n\pi/\tau_s}v_m$
III	$h\frac{\pi}{\tau_{dc}}+n\frac{\pi}{\tau_s}$	$\frac{1}{2}\cdot\frac{4F_{\max}}{h\pi}\Lambda_n$	$\frac{n\pi/\tau_s}{h\pi/\tau_{dc}+n\pi/\tau_s}v_m$

As shown in Fig.6, modular winding configuration adopts non-overlapped winding design to decouple coils of different phases. Therefore, the winding function of the armature winding in the modular machine, denoted as $N_{\mathrm{ac}}(x)$, equals to,

$$\begin{cases} N_{\mathrm{ac}}(x)=\sum_{k=1} N_k \sin(\frac{2\pi}{L_x}kP_{\mathrm{ac}}x) \\ N_k=\frac{1}{\pi kP_{\mathrm{ac}}}[1-\cos(\frac{2\pi}{L_x}kP_{\mathrm{ac}}\tau_m)]=\frac{2}{\pi kP_{\mathrm{ac}}}k_{pk} \end{cases} \tag{10}$$

where k is the order of winding function, P_{ac} is the pole-pair of the armature winding. Therefore, the phase flux linkages ψ_{m} are calculated as the sum of flux linkages at each side.

$$\begin{cases} \psi_m(t)=\psi_{m1}(t)+\psi_{m2}(t) \\ \psi_{m1}(t)=T_{\mathrm{ac}}l_{\mathrm{stk}}\int_0^{Lx}B_{\mathrm{dc1}}(x,t)N_{\mathrm{ac}}(x)dx \\ \psi_{m2}(t)=T_{\mathrm{ac}}l_{\mathrm{stk}}\int_0^{Lx}B_{\mathrm{dc2}}(x,t)N_{\mathrm{ac}}(x)dx \end{cases} \tag{11}$$

Substituting (8) (9) in (10), and using the simplification rule,

$$\begin{aligned} &\int_0^{Lx}\sin\{\frac{2\pi}{L_{\mathrm{x}}}[(hP_{\mathrm{dc}}\pm nP_{\mathrm{s}})x\pm nP_{\mathrm{s}}v_{\mathrm{m}}t)]\}\sin(\frac{2\pi}{L_{\mathrm{x}}}kP_{\mathrm{ac}}x)dx \\ &=\begin{cases} 0 & hP_{\mathrm{dc}}\pm nP_{\mathrm{s}}\neq kP_{\mathrm{ac}} \\ L_x/2\cos(\frac{2\pi}{L_{\mathrm{x}}}nP_{\mathrm{s}}v_{\mathrm{m}}t) & hP_{\mathrm{dc}}\pm nP_{\mathrm{s}}=kP_{\mathrm{ac}}>0 \\ -L_x/2\cos(\frac{2\pi}{L_{\mathrm{x}}}nP_{\mathrm{s}}v_{\mathrm{m}}t) & hP_{\mathrm{dc}}\pm nP_{\mathrm{s}}=-kP_{\mathrm{ac}}<0 \end{cases} \end{aligned} \tag{12}$$

Therefore, the phase flux linkages of one phase equals to (13),

$$\begin{aligned} &\psi_m(t)=\psi_{m1}(t)+\psi_{m2}(t) \\ &=\sum_{n=1,2,3...}\frac{1}{\pi}L_{stk}T_{ac}B_{h,n}k_{pk}\tau_w\cos(\frac{2\pi}{L_{\mathrm{x}}}nP_{\mathrm{s}}v_{\mathrm{m}}t) \\ &-\sum_{n=1,2,3...}\frac{1}{\pi}L_{stk}T_{ac}B_{h,n}k_{pk}\tau_w\cos(\frac{2\pi}{L_{\mathrm{x}}}nP_{\mathrm{s}}v_{\mathrm{m}}(t+\tau_{\mathrm{s}}/v_m)) \end{aligned} \tag{13}$$

where T_{ac} is the turns number of armature winding. τ_{w} is the working harmonics pitch. The phase voltage equals to (14),

$$\begin{aligned} &e_m(t)=e_{m1}(t)+e_{m1}(t) \\ &=\sum_{n=1,3,5...}2\cdot\frac{1}{\pi}\frac{2\pi}{L_{\mathrm{x}}}L_{stk}T_{ac}B_{h,n}k_{wk}\tau_w nP_{\mathrm{s}}v_{\mathrm{m}}\cos(\frac{2\pi}{L_{\mathrm{x}}}nP_{\mathrm{s}}v_{\mathrm{m}}t) \end{aligned} \tag{14}$$

Similarly, the inductance for the phase A is expressed as the sum of coils in upper module and lower module,

$$L_{\mathrm{m}}(t)=L_{\mathrm{m1}}(t)+L_{\mathrm{m2}}(t) \tag{15}$$

$$\begin{cases} L_{\mathrm{m1}}(t)=T_{\mathrm{ac}}l_{\mathrm{stk}}\int_0^{Lx}\Lambda_{\mathrm{s1}}(x,t)N_{\mathrm{ac}}^2(x)dx \\ \quad=L_0+\sum_{n=1,3,5...}^{\infty}L_n\sin(n\frac{\pi}{\tau_{\mathrm{s}}}v_{\mathrm{m}}t) \\ L_{\mathrm{m2}}(t)=T_{\mathrm{ac}}l_{\mathrm{stk}}\int_0^{Lx}\Lambda_{\mathrm{s1}}(x,t)N_{\mathrm{ac}}^2(x)dx \\ \quad=L_0+\sum_{n=1,3,5...}^{\infty}L_n\sin[n\frac{\pi}{\tau_{\mathrm{s}}}(v_{\mathrm{m}}t-\tau_{\mathrm{s}})] \end{cases}$$

where L_{m1} and L_{m2} are the inductance of the coils in the upper module and lower module, respectively. Furtherly, (15) can be further deduced to (15) as the odd harmonics are cancelled,

$$L_{\mathrm{m}}(t)=2L_0 \tag{16}$$

The electromagnetic force f_{em} of linear machines equals to the sum of dc-excited force f_{dc} and reluctance force f_{r} [18], which can be expressed as (17),

$$f_{\mathrm{em}}=f_{\mathrm{dc}}+f_{\mathrm{r}}=\frac{m}{2v_{\mathrm{m}}}(I_{\mathrm{ac}}\frac{\partial\psi_{\mathrm{m}}}{\partial t}+I_{\mathrm{ac}}^2\frac{\partial L_{\mathrm{m}}}{\partial t}) \tag{17}$$

where ψ_{m} is the phase flux linkages under no-load condition, I_{ac} is the armature current, L_{m} is the self-inductance in one phase. After substituting (12) and (14) into (16), the electromagnetic thrust of the machine can be derived. It can be perceived that after applying parallel-complementary design into this modular machine, the even-order harmonics of the dc-excited force could be eliminated effectively. Meanwhile, due to the constant phase inductance, the thrust ripples caused by saliency are eliminated as well. Therefore, thrust ripple of f_{em} can be suppressed.

III. DESIGN CONSIDERATION

A. Winding Factor Analysis

The feasible slot/pole combination for the proposed HMVF-LRM could be calculated by (18) [14], where m is the number of phases; j, i are positive integers; GCD is the great common divisor; N_{m} and N_{s} are the number of modules and secondary poles. For j=1, and i is an even integer, N_{m} is designed as 6, and N_{s} can be calculated as 8, 10, 14, etc. Similarly, for j=2 and i is an odd integer, N_{s} can be calculated as 11,13, etc.

$$\begin{cases} \frac{N_{\mathrm{m}}}{GCD(N_{\mathrm{m}},N_{\mathrm{s}})}=mj \\ N_{\mathrm{s}}=2N_{\mathrm{m}}\pm i \end{cases} \tag{18}$$

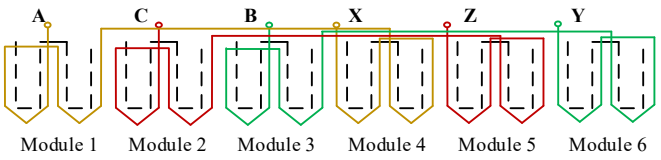

Fig. 6. Modular winding configuration of 6 modules.

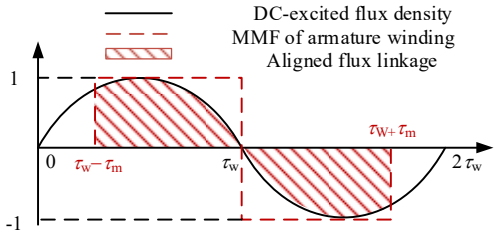

Fig.7. Pitch factor calculation of modular machine.

TABLE II INDUCED VOLTAGE GENERATION OF MODULAR DESIGN WITH DIFFERENT SLOT POLE COMBINATION

P_{dc}	P_s	(h,n)	P_{ac}	T_{ac}	k	P_w	τ_w	τ_s	G_r	$B_{h,n}$	k_{pn}	k_{dn}	v_m	E_{ph1}(*)	ΣE_{ph1}	FEA
6	10	(1, -1)	2	1	2	4	48.75	19.5	2.5	0.093	0.75	0.866	1	9.09	7.40	8.97
		(3, -1)	2	1	4	8	24.38	19.5	1.25	0.001	0.75	0.866	1	0.065		
		(1, 1)	2	1	8	16	12.19	19.5	0.63	-0.096	0.75	0.866	1	-2.33		
		(3, 1)	2	1	14	28	6.96	19.5	0.36	0.094	0.75	0.866	1	0.021		
6	11	(1, -1)	1	1	5	5	39	17.73	2.2	0.092	0.933	0.966	1	10.89	9.35	10.14
		(3, -1)	1	1	7	7	27.86	17.73	1.57	0.011	0.933	0.966	1	0.93		
		(1, 1)	1	1	17	17	11.47	17.73	0.65	-0.092	0.933	0.966	1	-3.23		
		(3, 1)	1	1	29	29	6.72	17.73	0.38	0.0089	0.933	0.966	1	0.18		
6	**13**	(1, -1)	1	1	7	7	27.86	15	1.86	0.084	0.933	0.966	1	8.40	**10.69**	**10.20**
		(3, -1)	1	1	5	5	39	15	2.6	0.024	0.933	0.966	1	3.40		
		(1, 1)	1	1	19	19	10.26	15	0.68	-0.043	0.933	0.966	1	-1.58		
		(3, 1)	1	1	31	31	6.29	15	0.42	0.021	0.933	0.966	1	0.47		
6	14	(1, -1)	2	1	4	8	24.375	13.93	1.75	0.079	0.75	0.866	1	5.38	7.85	8.90
		(3, -1)	2	1	2	4	48.75	13.93	3.5	0.026	0.75	0.866	1	3.55		
		(1, 1)	2	1	10	20	9.73	13.93	0.7	-0.082	0.75	0.866	1	-2.23		
		(3, 1)	2	1	16	32	6.09	13.93	0.44	0.024	0.75	0.866	1	0.41		

As illustrated in Figs. 6 and 7, the modular pitch factor of the working harmonics is calculated by two coils in one module. Therefore, the modular pitch factor is calculated as the integral about working harmonics from τ_w-τ_m to τ_w+τ_m, and equals to,

$$\begin{cases} k_{wn} = k_{pn} \cdot k_{dn} \\ k_{pn} = \dfrac{\pi}{4\tau_m} \cdot \int_{\tau_w-\tau_m}^{\tau_w+\tau_m} \sin(\dfrac{\pi}{\tau_w}x)dx = \dfrac{1}{2}(1-\cos\dfrac{\tau_m}{\tau_w}\pi) \\ k_{dn} = \dfrac{\sin(q\alpha_n/2)}{q\sin(\alpha_n/2)} \end{cases} \quad (19)$$

where τ_w is the pole pitch of working harmonics and τ_m is the pole pitch of one module.

Derived from (14) and (19), the fundamental amplitude of induced voltage can be expressed as (20),

$$E_{ph1} = 2T_{ac}l_{stk}v_m \sum_{P_w} \frac{\tau_w}{\tau_s} B_{h,n}(k_{dn}k_{pn}) \quad (20)$$

where k_{pk} and k_{dk} is the pitch factor and distribution factor of the kth armature harmonics, respectively, and $B_{h,n}$ is the amplitude of each working harmonics. According to (19), the major factors that determines the fundamental induced voltage in the armature winding can be classified into five categories, which are mover speed v_m, dimension parameters l_{stk}, τ_s, armature winding configuration, such as k_{dn}, k_{pn}, and T_{ac}, field densities parameters, such as $B_{h,n}$ and τ_w. The calculated induced voltage of modular machines with different slot/pole combinations can be summarized in Table II. It can be found that machines with 11 poles and 13 poles have higher winding factor for working harmonics, which reaches 0.933. The main contribution to the induced voltage is harmonics whose *h=1, n=-1*. Both the analytical and FEA calculation results proved that machines with 13 poles achieve higher induced voltage, which reach 10.69 and 10.20 mV/Turns. The FEA results agree with the analytical results calculated by (19) well.

B. Main Dimension Parameters and Optimization

The main geometric parameters of HMVF-LRM are illustrated in Fig.8. Furtherly, some coefficients inherited from main parameters are also defined as (21) to facilitate optimization, which impacts the thrust performance effectively.

$$k_{dc} = P_{loss(DC)} / (P_{loss(AC)} + P_{loss(DC)}) \quad (21\text{-a})$$

$$k_{sp} = \frac{2(h_s+g)}{h_m+2(h_s+g)} \quad (21\text{-b})$$

$$k_{sm} = w_{st1} / w_{mt} \quad (21\text{-c})$$

where $P_{loss(DC)}$ is copper loss of DC current, $P_{loss(AC)}$ is the copper loss of AC current. k_{sp} is split ratio of primary part of the machine, and k_{sm} is width of stator tips to mover tips. The calculation results are obtained by finite element method (FEM) and the transverse edge effect is neglected in the parametric analysis.

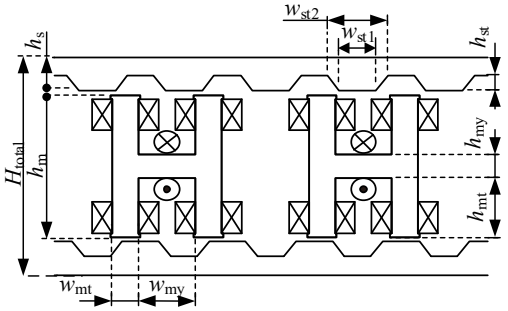

Fig.8. Geometric dimensions of the proposed machine.

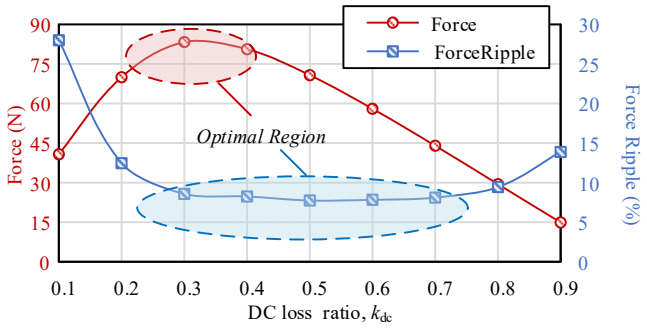

Fig. 9. Optimal region for DC loss ratio.

The impact of defined coefficients on thrust performance is assessed, as illustrated in Figs.9 and 10. The optimal ratio of DC copper loss, k_{dc} is achieved around 0.3, when copper loss of DC to AC reaches 1:2. This is because DC windings are wound on the yoke of the module, which makes both sides of the coil functional, and therefore the magnetic and electrical load are equally distributed for maximum output force. Furtherly, in this event, the optimal ratio of turns number of DC coils and AC coils is calculated as 2:1.

The optimal range of k_{sp}, is [0.3, 0.4], as shown in Fig.10. When k_{sp} increases furtherly, the space for secondary is suppressed, and the output force deceased due to the saturation problem in the stator. Meanwhile, the force ripple greatly increases as well. The optimal value for k_{sm} is around 1.2, when w_{st} is slightly larger than w_{mt}, as the flux leakage within this region is relatively low. The design parameters of the machine are summarized in TABLE. III, where initial values and optimal ranges of the variables are listed.

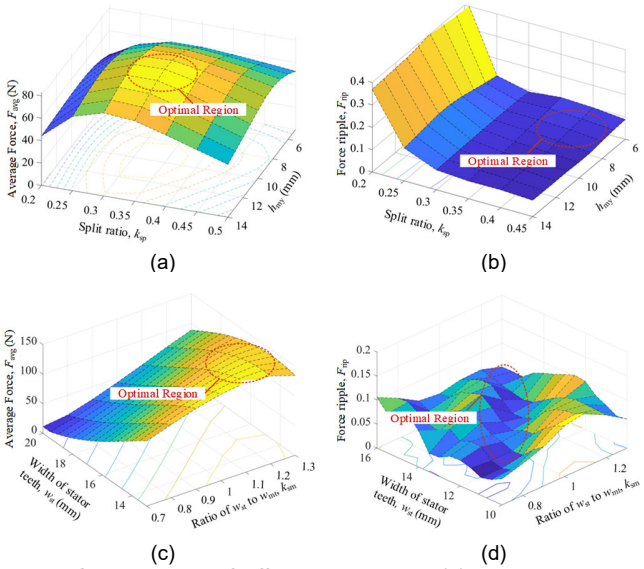

Fig. 10. Optimal region of different parameters. (a) F_{avg} v.s. k_{sp} and h_{my}. (b) F_{rip} v.s. k_{sp} and h_{my}. (c) F_{avg} v.s. w_{st} and k_{sm}. (d) F_{rip} v.s. w_{st} and k_{sm}.

TABLE III INITIAL DESIGN PARAMETER OF MVR-LRM

Symbol	Parameter	unit	Initial	Range
L_m	*Mover length*	mm	390	-
H_{total}	*Total height of the machine*	mm	82	-
g	*Airgap length*	mm	1	-
P_{loss}	*Copper loss*	W	180	-
J_e	*Current density*	A/mm^2	5.39	-
k_{sp}	*Split ratio*	-	0.3	[0.2, 0.5]
k_{dc}	*Ratio of DC to total loss*	-	0.3	[0.1, 0.9]
k_{sm}	*Ratio of stator teeth and mover*	-	1	[0.7, 1.3]
h_m	*Total height of the mover*	mm	56	[40, 64]
h_s	*Total height of the stator*	mm	24	[16, 40]
h_{my}	*Height of mover yoke*	mm	10	[6, 14]
w_{mt}	*Width of teeth tip*	mm	15	[10, 20]

Machine with forementioned four feasible different slot/pole combinations are optimized with a multi-objective genetic algorithm (MOGA). The objective of the machine is set as the average thrust and force ripple of the machine, which is defined as $(F_{max}- F_{min})/F_{avg}$*100%, and the maximum generation is set as 40, with 30 individuals in each generation. The algorithm basically contains three parts including optimal slot/pole combination, multi-objective genetic algorithm and non-dominated ranking. Furtherly, the motor is optimized with the MOGA algorithm under I_d=0 control algorithm, and all four motors are set as a fixed copper loss (180 W), mover length (390 mm) and stack length (50 mm). The optimal frontlines of four designs have been plotted in Fig.11. It turned out that a motor with 12/13 combination has higher average thrust force and less thrust ripple meanwhile. The motor with 12/13 slot/pole combination is selected for further study.

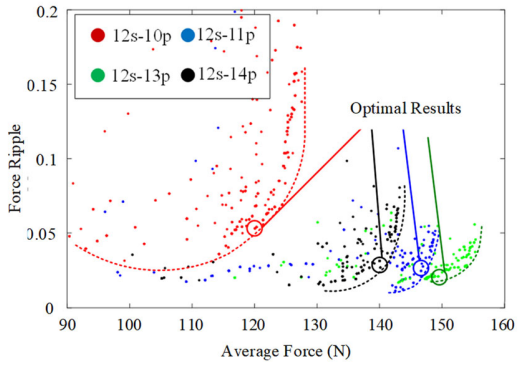

Fig. 11. Optimal results of different slot/pole combination.

IV. PERFORMANCE EVALUATION

A. Open-Circuit Performance of HMVF-LRM

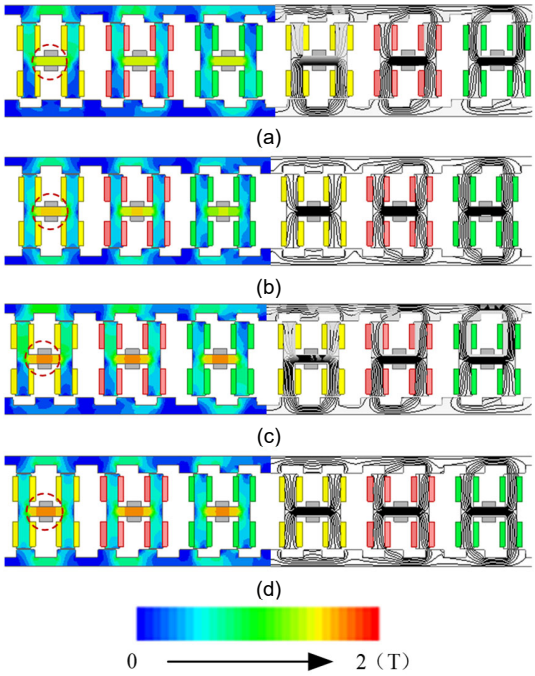

Fig.12 Open circuit flux density distribution. (a) Complementary structure with idc=6A. (b) Non-complementary structure with idc=6A. (c) Complementary structure with idc=12A. (d) Non-complementary structure with idc=12A.

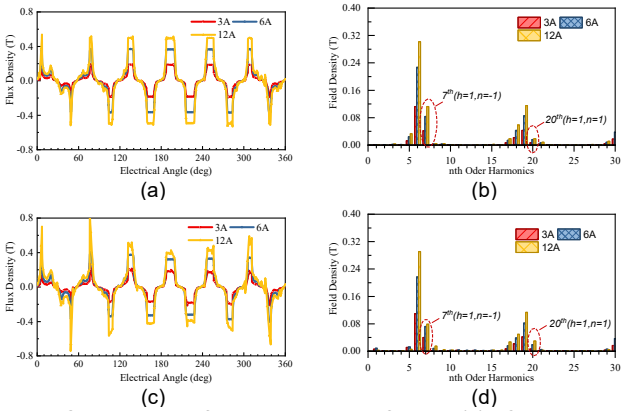

Fig.13 Open circuit flux density waveforms. (a) Complementary structure. (b) Conventional structure.

In this section, electromagnetic performance of the proposed DS-MVRLM with 12/13 slot/ pole combination is

evaluated via FEM with consideration of different excitation modes. Fig. 12 illustrates the open- circuit flux distributions with conventional structure and parallel-complementary structure under different excitations (i_{dc}=6A, 12A). As shown in the red dash circle in Fig. 12(a) and (b), it can be found that complementary structure could effectively relieve the saturation issue in the mover yoke. When the excitation current increases furtherly, the degree of saturation in the complementary design is lower than non- complementary counterparts.

Fig. 13 illustrates the waveform of flux distributions with conventional structure and parallel-complementary structure. As shown in Fig. 13, it can be found that after applying complementary structure, the waveform of flux density is effectively smoothed due to the relieving of saturation issue especially under over- excitation condition. In addition, the main working harmonic (7th- order) has also been boosted from 0.079T to 0.11T, when i_{dc}=12A.

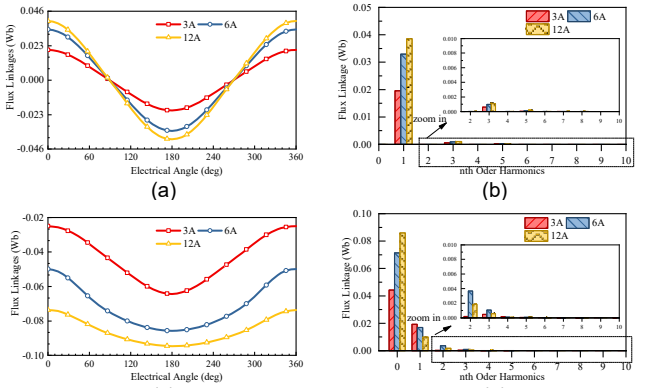

Fig. 14 Flux linkages distribution comparison. *(a) Waveforms of complementary structure. (b) Spectrum of complementary structure. (c) Waveforms of conventional structure. (d) Spectrum of conventional structure.*

Fig. 14(a) presents flux linkage waveforms of the machine with/ without complementary structure in one module and phase, whose spectrum via Fast Fourier Transform (FFT) is plotted in Fig. 14(b). Consistent with the theoretical analysis above, by applying complementary structure, even harmonics in flux linkages in one module and phase are effectively eliminated. Meanwhile, given the turns of AC winding is 58, the amplitude of flux linkages reaches 31.15 mWb and 17.32 mWb in complementary and conventional structure, respectively. The fundamental component of flux linkages is boosted over 79.87%. As the excitation current I_{dc} increases to 12A, the amplitudes of flux linkages in the winding A reach 38.52mWb. However, for conventional structure, the amplitude of flux linkages is decreased to 9.92 mWb.

Fig.15 presents calculated no-load back EMF of the proposed motor at speed of 2m/s. It can be found that even-order harmonics in phase has also been reduced effectively. Meanwhile, the phase induced voltage of the machine with complementary structure reach 26.08V, which is also 79.86% higher than that of machine without the complementary structure. The simulation results agree with the theoretical analysis in Section II A.

The complementary design furtherly reduced the detent force to a negligible degree, which is lower than 0.2N. Fig. 16 compares the value of the inductance of the machine, it can be seen that after applying complementary designs, the phase inductances fluctuates much less than the conventional counterpart, indicating the saliency of the machine is reduced. Therefore, it could also suppress the thrust ripple caused by reluctance force, when field orientated control (FOC) is applied. Thanks to the modular stator and winding configuration design, the mutual inductances between different phases are small enough to be neglected, indicating that each phase of the machine can work independently, and the fault tolerance of it can be strengthened accordingly.

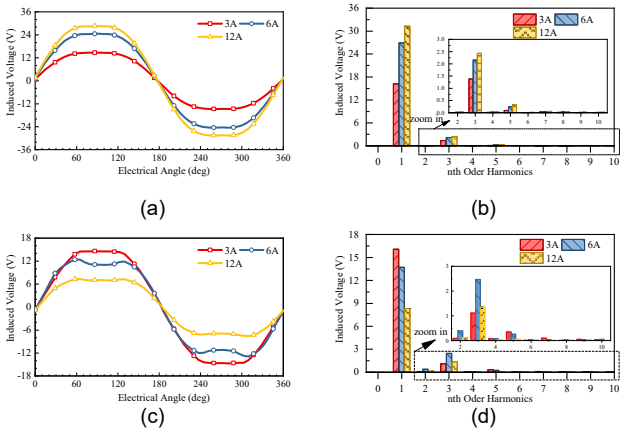

Fig. 15. Induced voltage comparison. *(a) Waveforms of complementary structure. (b) Spectrum of complementary structure. (c) Waveforms of conventional structure. (d) Spectrum of conventional structure.*

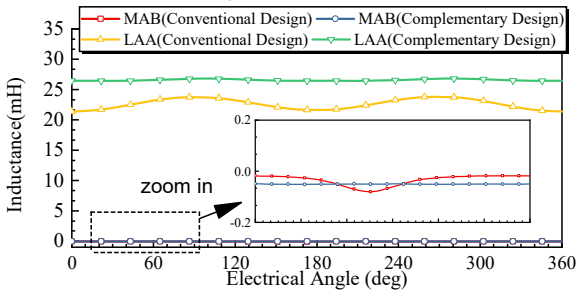

Fig. 16. Inductance comparison.

B. Thrust Characteristics

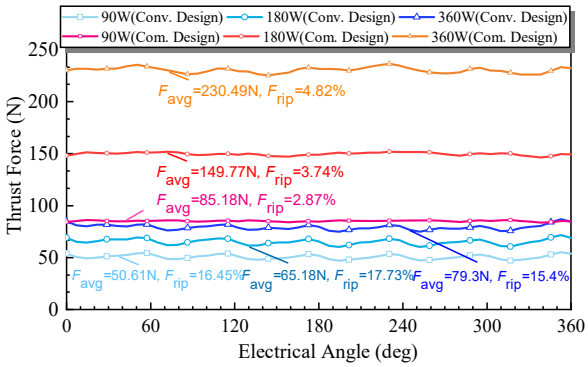

Fig.17. Rated output thrust characteristics.

The average thrust and thrust ripple of the machine with/ without complementary structure are compared under different copper loss in this part. Two machines with/ without complementary structure are simulated via FEA, and both of two machines are simulated under the same optimized parameters. Fig. 17 presents the rated output thrust of the two machines. It can be found that after applying complementary

structure to motor, the output thrust force of the motor has been improved from 65N to 148N at rated conditions, and the thrust ripple is also suppressed from 17.73% to 3.74%. Thanks to the complementary structure, the overload capability of motor with complementary design has been improved from 79.3N to 230.5N at heavy-loaded condition (360W). Meanwhile, the output thrust ripple is also suppressed, namely decreasing thrust ripple from over 18% to less than 5%. TABLE. V summarized the results of the two structures.

TABLE V COMPARISON OF MACHINES WITH/ WITHOUT COMP. STRUCTURE

	unit	Complementary Structure	without Comp. Structure
Mover length, L_m	mm	390	
Machine height, H_{total}	mm	82	
Stack Length, L_{stk}	mm	50	
Rated Current Density, J_e	A/mm^2	6.40	
Rated Speed, v[21]	m/s	2	
Thrust Force, F_t	N	150	65
Thrust Ripple Ratio, R_t	%	3.74	17.73
Output Power, P_2	W	300	130
Copper Loss, P_{cu}	W	180	
Iron Loss, P_{fe}	W	6.76	5.06
Efficiency, η	%	61.63	41.26
Output Power Density, ξ	kW/m^3	192.3	83.3

C. Fault Tolerant Performance

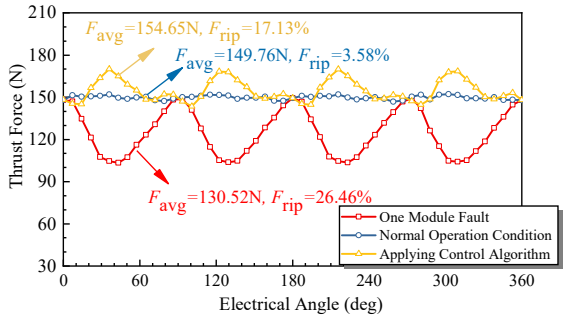

Fig.18. Fault-tolerant capability.

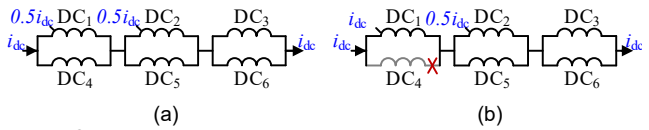

Fig.19 DC current distributions. *(a) Normal (b) Fault condition.*

Thanks to its modularized primary mover, the coupling effect between different phases has been relieved in the proposed HMVF-LRM, which benefits improving its fault tolerant capacity. Accordingly, the system is designed to be redundant, and the active fault tolerant control can be applied. Fig. 18 illustrates the thrust force of the machine when the fault in one module occurs. It can be found that, when the open circuit or short circuit occurs in one module, the average thrust force is reduced, and the ripple of the machine increases greatly. Meanwhile, as mentioned above, the fluctuations can be further smoothed after applying an active control algorithm. Fig. 19 demonstrates the DC current distribution under different conditions. It can be seen that when fault occurs in one module, the DC current in the other healthy module within the same phase will be doubled to make a power compensation [21]. In this way, the machine is also much more flexible for maintenance, which facilitates its WEC application.

D. Comparative Study

To verify the advantage of the proposed machine, a comparative study is performed among the proposed HMVF-LRM, conventional full- pitched variable flux linear reluctance machine (FP-VF-LRM), and modular switched reluctance linear machine (MSRLM), which is shown in Fig. 20. To make a fair comparison, all the machines in the part share the same mover length (L_m=390mm), total height (h_{total}=80mm) and copper loss (P_{loss}=180W). SLRM adopts semi-period conduction control, and the other two machines are controlled via field- oriented control (FOC). Other design parameters and their performance comparisons are listed in TABLE VI. As shown in TABLE VI, although MSRLM could achieve higher thrust force density, it still suffers from serious force ripple, which main cause vibration and other mechanical issues. Compared with conventional 12-10 full- pitched VF-LRM, the proposed machine obtains 41.30% higher thrust density and lower thrust ripple and higher power factor under the same copper loss. Furthermore, thanks to the modularized design, the fault tolerant capability of the machine is also strengthened.

TABLE VI PERFORMANCES COMPARISONS OF THREE MACHINES

Parameters	**Proposed**	**MSRLM** [8]	**VF-LRM**[22]
L_m, Mover teeth length (mm)		390	
w_{st}, Width of stator teeth (mm)	8.8	8.8	8.1
k_{sp}, Split ratio	0.69	0.69	0.74
k_{dc}, DC to total loss ratio	0.35	-	0.5
N_{ac}, Number of AC turns per coil	58	120	74
N_{dc}, Number of DC turns per coil	124	-	148
i_q, Q-axis RMS Current (A)	9.05	20.18	6.63
P_{loss}, Copper loss (W)		180	
f_t, Rated thrust force (N)	149.5	186.3	105.8
f_{rip}, Force ripple (%)	3.59	76.3	8.91
D_d, Thrust force density(kN/m^3)	95.83	119.4	67.84
pf, Power factor	0.4	-	0.38
Fault tolerant capability	good	good	poor

V. EXPERIMENTAL VERIFICATION

The prototype is manufactured based on the geometric parameters listed in TABLE III. DW540_50 is selected as the material for laminated iron of stator and mover, The rated speed is selected as 1m/s for the test. AWG 22 is selected for the copper wire. Fig.21 presents some details of the prototype. Fig. 21(a) shows the laminations of modular mover and long-rail stator. The locating hole is reserved for installation. The sole modular mover assembly is shown in Fig.21 (b). The concentrated windings simplify the winding process and boost the filling factor as well. Fig. 21(c) demonstrates the test platform for the prototype, which mainly consists of a servo linear motor, dynamometer, oscilloscope.

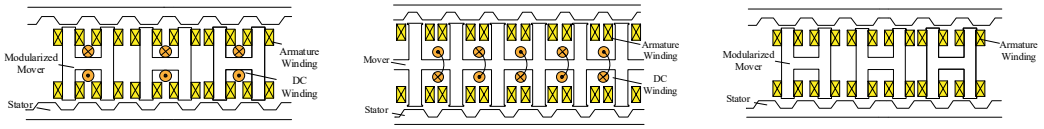

(a) (b) (c)

Fig. 20. Configuration of the three machines. (a) Proposed machine. (b) Conventional VF-LRM. (c) Modular SRLM.

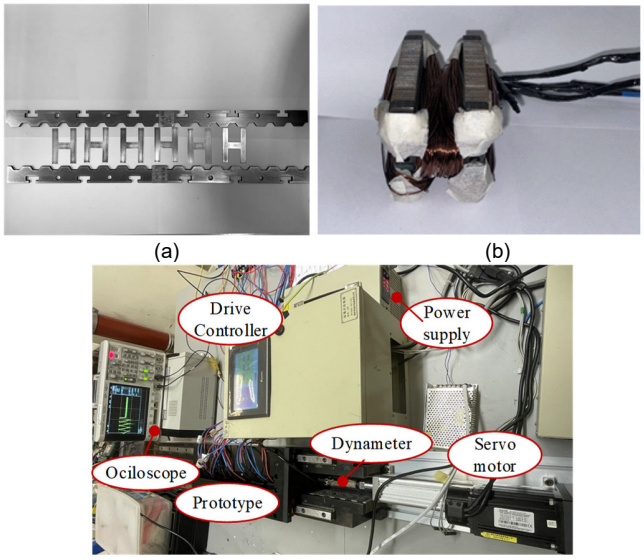

(a) (b) (c)

Fig. 21. HMVF-LRM prototype. *(a) Stator and mover lamination (b) Single module (c) Test platform*

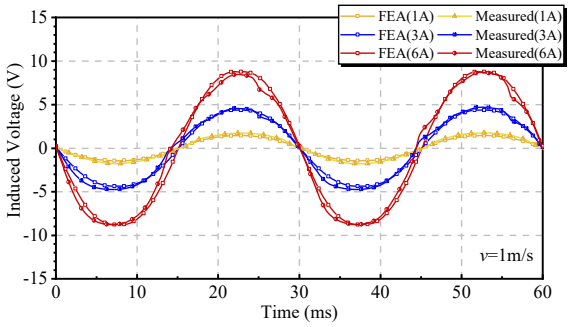

Fig. 22. Measured back EMF of phase A.

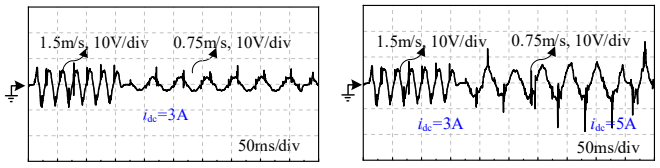

(a) (b)

Fig. 23. Measured flux regulation capability of the proposed machine. *(a) Unchanged excitation current. (b) Excitation current changed with different operation speed.*

As shown in Fig. 22, the open-circuit induced voltage is tested under the rated velocity of 1m/s, and DC current is set as 1A, 3A and 6A, respectively. Fig. 23 presents the flux regulation capability of the machine. Fig. 23 (a) shows the induced voltage of the machine at speed of 1.5m/s and 0.75m/s, when the DC field current equals to 3A. Fig.23 (b) shows the induced voltage of the machine at speed of 1.5m/s and 0.75m/s, and the DC field current also changes from 3A to 5A meanwhile. It is shown that by regulating the DC field current, the amplitude of output voltage of the machine could keep constant, which show its good flux regulation capability. Fig. 24 calculates the on-load test results of the machine under different power angles, when DC excitation current and effective value of AC (RMS) are set as 1A, 3A and 6A, respectively. The results show that the measured results basically agree with FEM results. The errors between FEA results and measured results are mainly caused by the dynameter when the pull force and push force are applied in sequence in a relatively short time interval.

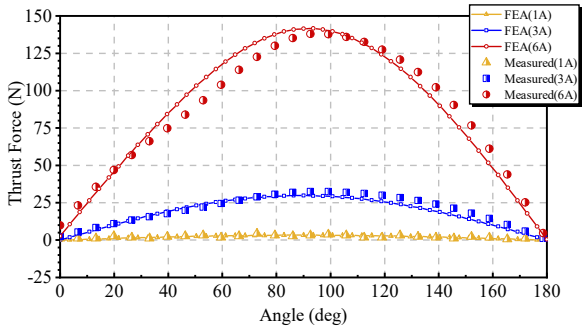

Fig. 24 Thrust characteristic test results.

VI. Conclusion

In this paper, an H-shaped modular variable flux linear reluctance machine is proposed. In summary, the proposed machine has the following characteristics,

1. The fault-tolerance capability of the machine has already been prompted effectively through modular design. The simulation shows that when one module is out of service, the thrust force of the machine is 130.52N and the thrust ripple rate is 26.46%. And the fluctuations can be further smoothed after applying a control algorithm to double the excitation current of the other module in the same phase.
2. By applying the complementary design to conventional modular-design-machine, the higher even-order harmonics have been suppressed effectively, and the thrust ripple of the machine has been well-relieved, whose thrust ripple ratio is suppressed as low as 3.59% after MOGA optimization.
3. According to EMC analysis of the machine, the parallel-complementary structure also effectively relieved the saturation problems in the core, and the heavy-load performance of the machine is prompted.
4. According to the quantitive harmonics analysis, modular machines with 6 modules/11poles (6m/11p) and 6modules/13 poles (6m/13p) possessing higher winding factor, and gear ratio G_r, could achieve higher induced voltage and output power. The spatial harmonics of 5th and 7th order plays main role in the modular machines of 6m/11p and 6m/13p.

5. Some design guidelines of the double-sided complementary-flux machine are proposed. The optimal ratio for DC to total power loss of the linear machine is approximately 0.3, and the optimal range of split ratio is around 0.3 to avoid partial saturation.

ACKNOWLEDGMENTS

This work was supported by the National Natural Science Foundation of China under Project 52077187 and in part by the Research Grant Council of the Hong Kong Government under Project PolyU 152143/18E and PolyU 152109/20E.

REFERENCES

[1] M. Leijon et al., "An electrical approach to wave energy conversion," Renewable energy, vol. 31, no. 9, pp. 1309-1319, 2006.
[2] Y. Shen, Z. Zeng, Q. Lu, and Y. Li, "Investigation of a Modular Linear Doubly Salient Machine with Dual-PM in Primary Yoke and Slot Openings," IEEE Transactions on Magnetics, vol. 55, no. 6, pp. 1-6, 2019.
[3] B.-S. Lee, H.-K. Bae, P. Vijayraghavan, and R. Krishnan, "Design of a linear switched reluctance machine," in Conference Record of the 1999 IEEE Industry Applications Conference. Thirty-Forth IAS Annual Meeting (Cat. No. 99CH36370), 1999, vol. 4, pp. 2267-2274: IEEE.
[4] J. Pan, Y. Zou, and G. Cao, "An asymmetric linear switched reluctance motor," IEEE Transactions on Energy conversion, vol. 28, no. 2, pp. 444-451, 2013.
[5] G. Stumberger, B. Stumberger, and D. Dolinar, "Identification of linear synchronous reluctance motor parameters," IEEE transactions on industry applications, vol. 40, no. 5, pp. 1317-1324, 2004.
[6] J. Ou, Y. Liu, M. Schiefer, and M. Doppelbauer, "A Novel PM-Free High-Speed Linear Machine With Amorphous Primary Core," IEEE Transactions on Magnetics, vol. 53, no. 11, pp. 1-8, 2017.
[7] T. W. Ching and W. Li, "A Superconducting Linear Variable Reluctance Machine for Urban Transportation Systems," IEEE Transactions on Applied Superconductivity, vol. 28, no. 3, pp. 1-5, 2018.
[8] W. Ding, S. Yang, Y. Hu, S. Li, T. Wang, and Z. Yin, "Design Consideration and Evaluation of a 12/8 High-Torque Modular-Stator Hybrid Excitation Switched Reluctance Machine for EV Applications," IEEE Transactions on Industrial Electronics, vol. 64, no. 12, pp. 9221-9232, 2017.
[9] W. Ding, H. Bian, K. Song, Y. Li, and K. Li, "Enhancement of a 12/4 Hybrid-Excitation Switched Reluctance Machine With Both Segmented-Stator and -Rotor," IEEE Transactions on Industrial Electronics, vol. 68, no. 10, pp. 9229-9241, 2021.
[10] D. Wang, X. Du, D. Zhang, and X. Wang, "Design, Optimization, and Prototyping of Segmental-Type Linear Switched-Reluctance Motor With a Toroidally Wound Mover for Vertical Propulsion Application," IEEE Transactions on Industrial Electronics, vol. 65, no. 2, pp. 1865-1874, 2018.
[11] D. Wang, Z. Feng, H. Zheng, and X. Wang, "Comparative Analysis of Different Topologies of Linear Switched Reluctance Motor with Segmented Secondary for Vertical Actuation Systems," IEEE Transactions on Energy Conversion, 2021.
[12] L. Szabó, "Advancements in electrical machines design brought by the modular construction," in 2018 X International Conference on Electrical Power Drive Systems (ICEPDS), 2018, pp. 1-6: IEEE.
[13] X. Li, X. Wang, and S. Yu, "Design and Analysis of a Novel Transverse-Flux Tubular Linear Switched Reluctance Machine for Minimizing Force Ripple," IEEE Transactions on Transportation Electrification, vol. 7, no. 2, pp. 741-753, 2021.
[14] M. Zheng, Z. Q. Zhu, S. Cai, and S. S. Xue, "A Novel Modular Stator Hybrid-Excited Doubly Salient Synchronous Machine with Stator Slot Permanent Magnets," IEEE Transactions on Magnetics, vol. 55, no. 7, pp. 1-9, 2019.
[15] G. Heins, D. M. Ionel, and M. Thiele, "Winding Factors and Magnetic Fields in Permanent-Magnet Brushless Machines with Concentrated Windings and Modular Stator Cores," IEEE Transactions on Industry Applications, vol. 51, no. 4, pp. 2924-2932, 2015.
[16] L. Wenlong, K. T. Chau, L. Chunhua, and Q. Chun, "Design and Analysis of a Flux-Controllable Linear Variable Reluctance Machine," IEEE Transactions on Applied Superconductivity, vol. 24, no. 3, pp. 1-4, 2014.
[17] T. W. Ching, Y. Shi, W. Li, and L. Jian, "Design and Analysis of a Magnetless Linear Variable Reluctance Motor With Modular Mover Units for Electric Propulsion," IEEE Transactions on Applied Superconductivity, vol. 30, no. 4, pp. 1-5, 2020.
[18] W. Zhao, J. Zhu, J. Ji, and X. Zhu, "Improvement of Power Factor in a Double-Side Linear Flux-Modulation Permanent-Magnet Motor for Long Stroke Applications," IEEE Transactions on Industrial Electronics, vol. 66, no. 5, pp. 3391-3400, 2019.
[19] T. Sheng and S. Niu, "Design of Doubly Complementary Stator-PM Machine With High Magnet Utilization Factor for Low-Cost Applications," IEEE Transactions on Energy Conversion, vol. 33, no. 2, pp. 567-575, 2018.
[20] Z. Li and S. Niu, "Design and analysis of a novel claw-shaped modular stator relieving-DC-saturation doubly salient machine with 3D complementary magnetic circuit," 2021.
[21] X. Zhao, S. Niu, X. Zhang and W. Fu, "Design of a New Relieving-DC-Saturation Hybrid Reluctance Machine for Fault-Tolerant In-Wheel Direct Drive," in IEEE Transactions on Industrial Electronics, vol. 67, no. 11, pp. 9571-9581, Nov. 2020.
[22] Y. Shen and Q. Lu, "Design and Analysis of Linear Hybrid-Excited Slot Permanent Magnet Machines," in IEEE Transactions on Magnetics, vol. 54, no. 11, pp. 1-6, Nov. 2018.